Human dynein-dynactin is a fast processive motor in living cells

Vikash Verma[1], Patricia Wadsworth[1,2,], and Thomas J. Maresca[1,2,]

[1] Biology Department, University of Massachusetts, Amherst

[2] Molecular and Cellular Biology Graduate Program, University of Massachusetts, Amherst

Correspondence to:

Thomas J. Maresca
Biology Department
University of Massachusetts, Amherst
Amherst, MA 01003
Phone: 413-545-0957
Fax: 413-545-3243
E-mail: tmaresca@umass.edu

Patricia Wadsworth
Biology Department
University of Massachusetts, Amherst
Amherst, MA 01003
Phone: 413-545-4877
Fax: 413-545-3243
E-mail: patw@umass.edu

Running title: Direct visualization of dynein-dynactin motility in human cells

ABSTRACT

Minus-end directed transport along microtubules in eukaryotes is primarily mediated by cytoplasmic dynein and its cofactor dynactin. Significant advances have been made in recent years characterizing human dynein-dynactin structure and function using in vitro assays, however, there is limited knowledge about the motile properties and functional organization of dynein-dynactin in living human cells. Total internal reflection fluorescence microscopy (TIRFM) of CRISPR-engineered human cells is employed here to visualize fluorescently tagged dynein heavy chain (DHC) and p50 with high spatio-temporal resolution. We find that p50 and DHC exhibit indistinguishable motility properties in their velocities, run lengths, and run times. The dynein-dynactin complexes are fast (~1.2 μm/s) and typically run for several microns (~2.7 μm). Quantification of the fluorescence intensities of motile puncta reveals that dynein-dynactin runs are mediated by at least one DHC dimer while the velocity is consistent with that measured for double dynein (two DHC dimers) complexes in vitro.

INTRODUCTION

The eukaryotic microtubule cytoskeleton plays a critical role in the organization, positioning and motility of organelles, mRNA, and proteins. Intracellular motility is mediated by molecular motor proteins that move cargoes along polarized microtubule tracks (for reviews see (Cason and Holzbaur, 2022; Reck-Peterson et al., 2018). The kinesin superfamily includes motors that are responsible for plus-end directed transport, and others that contribute to minus-end motility and regulation of microtubule dynamics (Hirokawa et al., 2009). In contrast, cytoplasmic dynein 1 motor complexes (hereafter dynein) (Canty et al., 2021; Pfister et al., 2005) are exclusively minus-end directed. The dynein complex is composed of two catalytic heavy chains, and additional light, light intermediate and intermediate chains (Carter et al., 2016; Cason and Holzbaur, 2022). The isolated dynein motor complex displays predominantly diffuse motility along microtubules in vitro, an observation that led to the identification of the dynactin complex, which is important for dynein motility (Gill et al., 1991; McKenney et al., 2014; Schlager et al., 2014; Schroer and Sheetz, 1991). In addition, a number of adaptor complexes that link dynein and dynactin to specific cargoes and activate the motor have been identified and characterized (Canty et al., 2021; Cason and Holzbaur, 2022; Reck-Peterson et al., 2018; Splinter et al., 2012).

Vesicular transport has been directly visualized by live-cell imaging in diverse cells including highly polarized axons (Canty et al., 2021). Motility of vesicles is bidirectional, both plus- and minus-end directed motors co-purify with cargoes, and adaptor complexes have been shown to associate with both kinesin and dynein motors (Ali et al., 2023; Hancock, 2014; Hendricks et al., 2010; Maeder et al., 2014; Vale, 1987). Together these observations indicate that the number and activity of cargo associated motors must be regulated to ensure efficient delivery to appropriate cellular destinations (Cason and Holzbaur, 2022). In vitro studies in which the number of motors bound to artificial cargoes can be precisely controlled demonstrate that cargoes with both plus and minus motors often stall or pause, or show directed motion that is distinct from either individual motor acting alone; however, once directed motion is initiated, reversals are

infrequent (Belyy et al., 2016; Derr et al., 2012). Cryo-EM of dynein-dynactin complexes revealed that the stoichiometry of dynein relative to dynactin is determined by the activating adaptors that link them. Specifically, the adaptor BICD2 recruited a single dynein to dynactin while BICDR1 and HOOK3 supported assembly of a “double dynein” complex (Chaaban and Carter, 2022; Grotjahn et al., 2018; Urnavicius et al., 2018; Urnavicius et al., 2015). Interestingly, the processivity and velocity of dynein-dynactin differs depending on the number of dyneins such that the double dynein complexes assembled with BICDR1 and HOOK3 had a higher frequency of processive motility events and moved faster than the single dynein complexes assembled with BICD2 (Urnavicius et al., 2018).

In contrast to the relative ease of visualizing motor proteins in in vitro motility assays, the crowded three-dimensional intracellular environment poses a challenge for imaging and quantifying motility events in living cells. In human cells constitutively over-expressing a GFP-tagged intermediate chain of dynein both dot-like, bidirectional motility and comet-like motile events, which co-localized with EB1, were observed, confirming a role for dynein in both tip-tracking and vesicle motility (Kobayashi and Murayama, 2009). Quantification of organelle motility in the highly polarized filamentous fungus *Ustilago maydis* expressing endogenously tagged fluorescent dynein revealed that binding of a single dynein to an anterograde-directed early endosome was sufficient to trigger directional reversal of its transport (Schuster et al., 2011).

In this study, HeLa cells expressing CRISPR/Cas9 modified dynein heavy chain (DHC) or the p50 subunit of dynactin were visualized using high-resolution fluorescence microscopy approaches to gain insights into the behaviors of dynein and dynactin in vivo. As a result, we were able to directly observe and quantify core motility parameters of dynein-dynactin while analyses of their fluorescence intensities relative to a known standard was informative of the stoichiometry of dynein in motile dynein-dynactin complexes in proliferating human cells.

67 **RESULTS AND DISCUSSION**

68 Human HeLa cells were engineered using CRISPR/Cas9 to insert a cassette encoding FKBP and
69 EGFP tags in frame at the 3' end of the dynein heavy chain (DYNC1H1) gene (SF1). A clonal
70 DHC-EGFP-expressing HeLa cell line was generated and subjected to live-cell fluorescence
71 imaging to directly visualize DHC activities in interphase cells. The most striking dynein behavior
72 was tip-tracking on polymerizing MTs as an abundance of DHC comets traveling at the speed of
73 MT polymerization (Cassimeris et al., 1988; Rusan et al., 2001; Walker et al., 1988) were readily
74 observed by both spinning disc confocal microscopy and total internal reflection fluorescence
75 microscopy (TIRFM) (**Fig. 1 A, B, Videos 1 and 2**). SiR-Tubulin was next introduced to visualize
76 DHC localization and behaviors relative to MTs (**Fig. 1 C**). Interestingly, because SiR-Tubulin is
77 a docetaxol derivative, its addition suppressed plus-end MT polymerization resulting in a
78 significant reduction in the DHC tip-tracking population and a much clearer view of a different
79 population of MT-associated DHC puncta (**Fig. 1 C**). The SiR-Tubulin-treated cells were subjected
80 to two-color TIRFM to determine if the DHC puncta exhibited motility and; indeed, puncta were
81 observed streaming along MTs, which was especially evident via TIRFM on MTs that were pinned
82 between the nucleus and the plasma membrane (**Video 3**). DHC puncta were next visualized with
83 higher temporal resolution by acquiring single color TIRFM time-lapses of the EGFP channel at a
84 rate of 5 frames per second (fps) (**Fig. 1 D, Video 4**). The TIRFM time-lapses were assessed by
85 eye and several parameters of the motile puncta were measured using kymographs (**Fig. 1 E**).
86 The average DHC puncta moved at 1.2 ± 0.05 (mean ± SEM) μm/sec over a distance of 2.8 ± 0.2
87 μm for 2.6 ± 0.2 seconds (**Fig. 1 F-H**). While some motile puncta appeared to switch "tracks" at
88 MT intersections, which was inferred from observations of sudden high angle turns, directional
89 switches on the same MT were infrequent (~5-10% of runs). It should also be noted that the run
90 lengths and run times for DHC are likely underestimates as the puncta could only be tracked while
91 they remained in the TIRFM evanescent field and prior to their photobleaching.

92 Activation of dynein motility requires its interaction with the dynactin complex (Chowdhury
93 et al., 2015; Grotjahn et al., 2018; Urnavicius et al., 2018; Zhang et al., 2017). CRISPR/Cas9-
94 based genomic engineering was used to insert the cassette encoding FKBP and EGFP tags at
95 the 3' end of the p50/dynamitin gene and a clonal p50-EGFP-expressing HeLa cell line was
96 subjected to live-cell fluorescence imaging to visualize dynactin in interphase cells. Consistent
97 with prior observations of dynactin localization (Vaughan et al., 1999; Vaughan et al., 2002) and
98 like dynein, dynactin exhibited robust tip-tracking activity on growing MT plus-ends that was
99 clearly visualized via both spinning disc confocal imaging and TIRFM (**Fig. 2 A, B; Videos 5 and**
100 **6**). Suppression of plus-end polymerization dynamics upon introduction of SiR-Tubulin caused a
101 loss of the tip-tracking pool of dynactin, which made a second pool of motile, MT-associated
102 puncta of p50 more pronounced especially when visualized with TIRFM (**Fig. 2 C, Video 7**). The
103 p50-EGFP-expressing cells were then subjected to single color TIRFM at 5 fps and kymograph
104 analysis to measure the motility parameters of the dynactin complex (**Fig. 2 D**). The mean velocity
105 of the p50 puncta was 1.2 ± 0.07 μm/sec (**Fig. 2 E**) while the mean run length was 2.6 ± 0.2 μm
106 (**Fig. 2 F**) and the mean run time was 2.2 ± 0.2 seconds (**Fig. 2 G**). Similar to dynein, dynactin
107 was observed to switch MT "tracks" but infrequently switched direction.

108 In comparing the motility parameters of the motile dynein and dynactin puncta, their
109 velocities (**Fig. 3 A**), run lengths (**Fig. 3 B**), and run times (**Fig. 3 C**) were statistically
110 indistinguishable. Thus, we inferred that the motile population of dynein was associated with the
111 dynactin complex. The fluorescence intensities of motile DHC and p50 puncta were next
112 compared to EGFP-tagged kinesin-1 dimer as a standard to assess the stoichiometries of the
113 motile dynein and dynactin complexes (**Fig. 3 D-F**). Interestingly, the intensity of motile DHC-
114 EGFP puncta was not statistically significantly different from the intensity of motile kinesin-1-
115 EGFP dimers; however, the intensity of motile p50 puncta had a mean fluorescence intensity that
116 was about half that of the motile kinesin-1-EGFP puncta (**Fig. 3 G**). Thus, the motile dynein and
117 dynactin complexes visualized here via high-speed TIRFM were comprised, on average, of two

118 EGFP-tagged DHC molecules and a single p50-EGFP molecule. When considering how these
119 values relate to physiological stoichiometries of the motile dynein-dynactin complexes, it is
120 important to note that both the DHC-EGFP and p50-EGFP HeLa cell line clones are
121 heterozygotes (**Fig. 3 H, I**). Dynein motility requires DHC dimerization and if there is an equal
122 likelihood of EGFP-tagged and untagged DHC incorporation into a functional dimer then the
123 motile dynein puncta we visualized would actually contain two DHC dimers. While we were unable
124 to assess the relative expression levels of tagged versus untagged DHC for technical reasons,
125 we can confidently conclude from our data that there is at least one DHC dimer in the motile
126 puncta. Interestingly, western blotting of cell extract prepared from the p50-EGFP clone revealed
127 that the cells expressed a ~5-6-fold molar excess of the untagged p50 compared to p50-EGFP
128 (**Fig. 3 I**). Differential allele regulation has been observed for endogenously tagged proteins
129 (Mann and Wadsworth, 2018; Roberts et al., 2017) suggesting that regulation of gene expression
130 may help avoid deleterious effects when cells can tolerate a fraction of the total protein pool being
131 modified. The relative levels of EGFP-tagged versus untagged p50 most likely explains why motile
132 p50 puncta only had a single EGFP molecule despite the fact that the dynactin complex is known
133 to have four copies of p50 (Eckley et al., 1999; Urnavicius et al., 2015). Thus, we conclude that
134 the motile dynactin complexes visualized here are typically comprised of one p50-EGFP molecule
135 and 3 untagged copies of p50.

136 While several groups have recently imaged endogenously tagged dynein in mitotic HeLa
137 cells and iNeurons (Fellows et al., 2023; Ide et al., 2023), to our knowledge - this is the first direct
138 visualization of motile endogenously-tagged human dynein-dynactin complexes in proliferating,
139 non-neuronal cells. Two distinct motile populations of dynein-dynactin exist in human interphase
140 cells: one pool that tip-tracks on polymerizing MT plus-ends and a second pool that moves
141 processively at high velocities (~7X faster than the tip-tracking population) along MTs. We
142 propose that the ~3 μm run lengths measured here are an underestimate of what the dynein-
143 dynactin complex is capable of due to the relatively short and dynamic MT tracks available to it in

144 interphase HeLa cells and because motile puncta could only be visualized while they were in the
145 TIRF field and prior to their photobleaching. Indeed, dynein was recently shown to be incredibly
146 processive in iNeurons where its mean run length was ~ 35 μm and runs >100 μm were observed
147 (Fellows et al., 2023). It is possible that the tip-tracking pool of dynein-dynactin is regulated in a
148 cell-cycle dependent manner because dynein-dynactin tracking events were less robust in mitotic
149 cells than in interphase cells. The dynein-dynactin pool that exhibited directional motility on MTs
150 was capable of switching MT tracks but rarely switched directions suggesting that there is not a
151 constant tug-of-war between dynein-dynactin and kinesins in proliferating cells as compared to
152 observations of bidirectional vesicular transport in neurons (Hancock, 2014; Hendricks et al.,
153 2010; Maeder et al., 2014). The low directional switching frequency observed here is consistent
154 with in vitro studies reconstituting the tug-of-war phenomenon showing that one type of motor
155 dominates once directional movement begins and that reversal events are rare (Ali et al., 2023;
156 Belyy et al., 2016; Derr et al., 2012). The velocities measured here in HeLa cells were comparable
157 to those measured for unopposed dynein and; therefore, did not suggest that there was significant
158 resistive drag from associated kinesin motors as has been observed in vitro. This suggests that
159 the cargos, which we presume motile dynein-dynactin puncta are bound to, any kinesins
160 associated with the cargos are inactive and/or cannot effectively bind the MT lattice during dynein-
161 dynactin-mediated transport in interphase HeLa cells. Interestingly, directional switching was also
162 uncommon during retrograde dynein-dynactin movements in iNeuron axons (Fellows et al., 2023)
163 and in retrograde trafficking of early endosomes in *Ustilago maydis* mediated by dynein-dynactin
164 containing the HOOK3 adaptor (Bielska et al., 2014; Schuster et al., 2011).

165 Dynein-dynactin motility is also affected by tubulin modifications (Barisic and Maiato,
166 2016; Roll-Mecak, 2020; Sirajuddin et al., 2014) most notably by the tyrosination state of α-tubulin
167 such that dynein-dynactin preferentially associates with tyrosinated MTs to promote the initiation
168 of motility (McKenney et al., 2016; Nirschl et al., 2016; Peris et al., 2006). Since all of the motility

169 parameters reported here were measured for dynein-dynactin walking on docetaxol-stabilized
170 MTs it is likely that the MT lattice was more detyrosinated than normal in our experimental
171 conditions (Gundersen et al., 1987; Webster et al., 1990). Thus, it would be informative to apply
172 our high resolution TIRFM imaging of dynein-dynactin in cells where tubulin modifications –
173 starting with the tyrosination state – can be experimentally manipulated (Barisic et al., 2015;
174 Ferreira et al., 2020).

175 Finally, our cell-based data are consistent with recent in vitro characterizations of dynein-
176 dynactin structure, function, and regulation (Belyy et al., 2016; Chaaban and Carter, 2022;
177 Urnavicius et al., 2018). Based on our fluorescence intensity measurements, we favor the
178 interpretation that the motile dynein-dynactin complexes visualized here are typically comprised
179 of a single dynactin complex bound to a tandem array of two dyneins. Our measured dynein-
180 dynactin velocity of 1.2 μm/sec further supports this conclusion since this speed is consistent with
181 in vitro velocities of dynein-dynactin complexes containing activating adaptors that recruit two
182 dyneins although we do not exclude that the range of DHC velocities and intensities measured
183 here may include sub-populations of dynein-dynactin containing a single dynein dimer. It would
184 be valuable to test whether dynein-dynactin regulation mechanisms that have been characterized
185 in vitro also apply to the physiological regulation of dynein-dynactin activity in living cells by
186 measuring DHC motility parameters and intensities in cells depleted of different cargo adaptors.
187 Ultimately, we hope that the direct visualization of human dynein-dynactin and quantification of
188 its motility parameters and stoichiometries in living cells will be an important physiological
189 complement to in vitro assays, which altogether will better inform mechanistic models of the many
190 cellular processes that rely on dynein-dynactin.

191

192

193 **MATERIALS AND METHODS**

194 **Cell culture**

195 Parental HeLa and CRISPR-edited HeLa clones expressing DHC-EGFP or p50-EGFP were
196 grown in standard DMEM medium (Gibco, USA) supplemented with 10% non-heat-inactivated
197 FBS (Gibco, USA) and 0.5× antibiotic/antimycotic cocktail (Sigma-Aldrich) and maintained at
198 37°C with 5% CO2. Human-Kinesin-1-EGFP-expressing *Drosophila* S2 cells were grown in
199 Schneider's medium (Life Technologies) supplemented with 10% heat inactivated fetal bovine
200 serum (FBS) and 0.5x antibiotic/antimycotic cocktail (Sigma), and maintained at 25°C. Kinesin-1-
201 EGFP expression was induced with 500μM $CuSO_4$ for 16-18 hours.

202

203 **CRISPR-engineered cell line production**

204 *CRISPR gene editing.*

205 FKBP-EGFP tags were added to the C-terminus of human dynein heavy chain (DHC) and p50
206 using methods described previously (Sheridan and Bentley, 2016; Stewart-Ornstein and Lahav,
207 2016). In brief, repair cassettes comprised of FKBP-EGFP linked to a cleavable peptide (T2A)
208 followed by a selectable marker (Neomycin) were cloned into pCMV and used for PCR reactions.
209 Glycine-Alanine linkers were included between proteins in the construct. Guide sequences were
210 selected using the CRISPR design tool (http://crispr.mit.edu/) from the Zhang lab at MIT (Ran et
211 al., 2013) using "other regions" and the human target genome (hg19). The search tool was used
212 to select guides close to the C-terminus of the protein of interest (~100nt surrounding and
213 including the stop codon). Top and bottom oligos were obtained for each guide with the bases 5'-
214 CACC -3'added to the top oligo and 5'-AAAC-3' added to the complement of the bottom oligo.

215 Guides were cloned into a Cas9 containing plasmid (PX459) Addgene #62988,
216 (Cambridge, MA) following methods previously outlined (Moyer and Holland, 2015). Top and
217 bottom oligos were annealed and then phosphorylated by T4 PNK (NEB, Ipswich, MA). Guides
218 were then cloned into PX459 that was cut using BbsI (NEB, Ipswich, MA) and ligated using T4

219 ligase (NEB Ipswich, MA). Guide-Cas9 containing plasmids were then sequenced using the U6
220 promotor primer (Ran et al., 2013) and purified using either endotoxin free mini-preps or midi-
221 preps according to manufacturer protocol (Promega, Madison, WI). Repair cassettes were
222 amplified using primers designed to be homologous to the C-terminal genomic DNA surrounding
223 the STOP codon. In all cases, the guide target sequence was mutated to prevent Cas9 from
224 recognizing the repair cassette.

225 Cells were grown in DMEM medium (ThermoFisher Scientific) with 10% Fetal bovine
226 serum (FBS, Atlanta Biologicals, Flowery Branch, GA) and 0.5X antibiotic/antimycotic solution
227 (final concentrations 50 U/mL penicillin, 0.05 mg/mL streptomycin, 0.125 ug/mL amphotericin B;
228 Sigma-Aldrich, St. Louis, MO) at 37 °C and 5% carbon dioxide (CO_2). For long term storage cells
229 were frozen in DMEM medium with 5% FBS and 0.5X antibiotic/antimycotic solution and 15%
230 DMSO and held at -80°C for 1-2 days before moving to liquid nitrogen.

231 To generate CRISPR modified cell lines, parental cells were nucleofected using an Amaxa
232 Nucleofector (Lonza, Portsmouth, NH) program I-013 and Mirus nucleofection reagent (Mirus Bio
233 LLC, Madison, WI) according to the manufacturer's recommendations. Plasmids and Repair
234 cassettes were used at ratio of 1:1 at a concentration of 1 µg DNA each. Following nucleofection,
235 cells were grown in regular growth media in 100mm dishes for 48-72 Hrs. and then 0.2g/L
236 Neomycin/G418 (InvivoGen, San Diego, CA) selection media was added. Media was then
237 changed daily for 10-14 days and colonies of green cells were picked using cloning rings and
238 returned to regular media for further screening and experiments.

239

240 *Genotyping*

241 Genomic DNA was isolated from clonal CRISPR tagged cells using Genomic DNA Mini Kit
242 (Invitrogen) according to manufacturer's recommendations. DNA was then amplified by PCR
243 using genomic primers targeting the Neomycin cassette- and downstream of the Stop codon.
244 Phusion polymerase (NEB) was used to amplify 1 µL of isolated genomic DNA in a 50 µL reaction

245 for 30 cycles. The resulting PCR products were analyzed using 0.8% agarose gel
246 electrophoresis. The expected band was excised, and gel extracted using Qiagen gel extraction
247 kit and sequenced to verify proper integration of the tag.
248
249 **Live-cell TIRF microscopy (TIRFM)**
250 Cells were seeded onto 35 mm glass bottom petri dishes (Cellvis) 2-3 days prior to imaging. With
251 the exception of the visualization of tip-tracking DHC-EGFP, cells were incubated in MEDIA
252 supplemented with 1 μM SiR-Tubulin (Cytoskeleton, Inc) for 30-60 minutes prior to washing out
253 the SiR-Tubulin with fresh DMEM before imaging. The cells were visualized on a Nikon Ti-E
254 microscope equipped with a TIRF illuminator, a 100X 1.49-NA differential interference contrast
255 TIRF Apochromat oil-immersion objective, Nikon perfect focus system (PFS), a Hamamatsu
256 ORCA-Flash 4.0 LT digital complementary metal-oxide semiconductor camera (C11440), four
257 laser lines (447, 488, 561, and 641 nm), and MetaMorph software (Molecular Devices). Flat
258 interphase cells were identified and the initial focal plane was set by focusing on the far-red SiR
259 tubulin signal with a particular emphasis on finding cells in which individual microtubules could be
260 seen between the nucleus and the glass-adhered plasma membrane. Individual snap shots were
261 then taken on the EGFP channel to refine the focal plane on the DHC or p50 puncta. Once
262 individual puncta were well-resolved the PFS was engaged and the cell was subjected to
263 streaming TIRFM for 12 seconds at an acquisition rate of 5 frames per second (200 ms exposure)
264 and 2x2 camera binning.
265
266 **Quantifications of motility parameters and fluorescence intensities**
267 High temporal (5 fps) TIRFM time-lapses were examined by eye to identify evident motile puncta,
268 the paths of which were traced manually in MetaMorph using the Multi-Line drawing function. A
269 kymograph of the line segment with a 5-pixel line width was then generated and the velocity was
270 determined by measuring the slope of the motility event on the kymograph from start to end using

271 the Single Line drawing function. The run time was measured by defining the start and end frame
272 of evident movement in the TIRFM time-lapse and the run length was then calculated by
273 multiplying the run time by the velocity measured in the kymograph of the motility event. The run
274 times and run lengths are likely underestimates of what dynein-dynactin can achieve due to the
275 fact that the puncta sometimes bleached or exited the TIRFM evanescent field.

276 The number of EGFP molecules per motile puncta of DHC and p50 was determined by
277 comparing their background-corrected fluorescence intensities to that of a known dimer standard:
278 human kinesin-1 tagged with EGFP. As previously described (Ye et al., 2018) *Drosophila* S2 cells
279 expressing inducible human Kinesin-1 (in this case tagged with EGFP) were induced with 500μM
280 CuSO4 for 16 hours to induce expression. The next day, the induced S2 cells were seeded onto
281 a concanavalin A coated glass bottom petri dish and allowed to adhere for ~1 hour prior to
282 visualization by TIRFM. The DHC-EGFP and p50-EGFP HeLa clones and the human Kinesin-1-
283 EGFP-expressing S2 cells were each visualized sequentially via live-cell TIRF microscopy using
284 identical imaging parameters (5 fps acquisition rate, 200 ms exposure, 2X2 binning) within the
285 same region of the camera chip. The region-in-region method (Ye and Maresca, 2018) was then
286 used to background correct and quantify the integrated fluorescence intensities of motile puncta
287 of DHC-, p50-, and kinesin-1-EGFP in the same TIRFM time-lapses that were used to measure
288 the motility parameters. The intensity of each motile puncta was measured for a single time-point
289 from each run in which the spot was most clearly resolved and did not have significant local
290 background signal from nearby EGFP puncta.

291

292 **Western blotting**

293 Twenty μg of total protein from cell lysates prepared from parental HeLa cells or the p50-EGFP
294 clone were loaded onto a 10% SDS-PAGE gel, run out, and transferred to a nitrocellulose
295 membrane on the Trans-Blot® Turbo™ transfer system (Bio-Rad Laboratories) using the
296 preprogrammed “HIGH MW” 10-minute protocol. After blocking for 1 hour in TBS with 0.1% Tween

297 and 5% milk, the membrane was incubated overnight at 4°C with mouse anti-dynactin p50 (BD
298 Transduction Laboratories, Cat. # 611002) diluted at 1:1000 in the block. The membrane was
299 washed 3X 5 minutes in TBS + 0.1% Tween and then incubated for 1 hour in milk containing
300 donkey-anti-mouse IgG secondary antibodies conjugated with HRP (Jackson ImmunoResearch
301 Laboratories, Inc.) diluted at 1:5000 in block. Following 3X 5 minutes washes in TBS + 0.1%
302 Tween the blot was incubated with Immobilon Western Chemiluminescent HRP Substrate
303 (Millipore) according to the manufacturer's recommendations. Imaging of the membrane was
304 done on a G:Box system controlled by GeneSnap software (Syngene).
305

306 **Statistical analyses**

307 Statistical analyses reporting p-values from two-tailed Student's t-tests were done in excel while
308 p-values generated with the randomization method were done using the PlotsofDifferences web
309 tool at: https://huygens.science.uva.nl/PlotsOfDifferences (Goedhart, 2019). PlotsofDifferences
310 does not rely on assumptions about the distribution of the data (normal versus non-normal) to
311 calculate p-values.
312

313 **ACKNOWLEDGMENTS**

314 We are grateful to Barbara Mann for generating the CRISPR-engineered HeLa cell lines. This
315 work was supported by an NIH grant (GM107026) to T.J.M. and by an NSF grant (MCB1817926)
316 to P.W.

317

318 **CONFLICT OF INTEREST**

319 The authors declare no competing financial interests.

320
321

REFERENCES

Ali, F.A., A.J. Zwetsloot, C.E. Stone, T.E. Morgan, R.F. Wademan, A.P. Carter, and A. Straube. 2023. KIF1C activates and extends dynein movement through the FHF cargo adaptor. *bioRxiv*:2023.2010.2026.564242.

Barisic, M., and H. Maiato. 2016. The Tubulin Code: A Navigation System for Chromosomes during Mitosis. *Trends Cell Biol*. 26:766-775.

Barisic, M., R. Silva e Sousa, S.K. Tripathy, M.M. Magiera, A.V. Zaytsev, A.L. Pereira, C. Janke, E.L. Grishchuk, and H. Maiato. 2015. Mitosis. Microtubule detyrosination guides chromosomes during mitosis. *Science*. 348:799-803.

Belyy, V., M.A. Schlager, H. Foster, A.E. Reimer, A.P. Carter, and A. Yildiz. 2016. The mammalian dynein-dynactin complex is a strong opponent to kinesin in a tug-of-war competition. *Nat Cell Biol*. 18:1018-1024.

Bielska, E., M. Schuster, Y. Roger, A. Berepiki, D.M. Soanes, N.J. Talbot, and G. Steinberg. 2014. Hook is an adapter that coordinates kinesin-3 and dynein cargo attachment on early endosomes. *J Cell Biol*. 204:989-1007.

Canty, J.T., R. Tan, E. Kusakci, J. Fernandes, and A. Yildiz. 2021. Structure and Mechanics of Dynein Motors. *Annu Rev Biophys*. 50:549-574.

Carter, A.P., A.G. Diamant, and L. Urnavicius. 2016. How dynein and dynactin transport cargos: a structural perspective. *Curr Opin Struct Biol*. 37:62-70.

Cason, S.E., and E.L.F. Holzbaur. 2022. Selective motor activation in organelle transport along axons. *Nat Rev Mol Cell Biol*. 23:699-714.

Cassimeris, L., N.K. Pryer, and E.D. Salmon. 1988. Real-time observations of microtubule dynamic instability in living cells. *J Cell Biol*. 107:2223-2231.

Chaaban, S., and A.P. Carter. 2022. Structure of dynein-dynactin on microtubules shows tandem adaptor binding. *Nature*. 610:212-216.

Chowdhury, S., S.A. Ketcham, T.A. Schroer, and G.C. Lander. 2015. Structural organization of the dynein-dynactin complex bound to microtubules. *Nat Struct Mol Biol*. 22:345-347.

Derr, N.D., B.S. Goodman, R. Jungmann, A.E. Leschziner, W.M. Shih, and S.L. Reck-Peterson. 2012. Tug-of-war in motor protein ensembles revealed with a programmable DNA origami scaffold. *Science*. 338:662-665.

Eckley, D.M., S.R. Gill, K.A. Melkonian, J.B. Bingham, H.V. Goodson, J.E. Heuser, and T.A. Schroer. 1999. Analysis of dynactin subcomplexes reveals a novel actin-related protein associated with the arp1 minifilament pointed end. *J Cell Biol*. 147:307-320.

Fellows, A.D., M. Bruntraeger, T. Burgold, A.R. Bassett, and A.P. Carter. 2023. Dynein and dynactin move long-range but are delivered separately to the axon tip. *bioRxiv*:2023.2007.2003.547521.

Ferreira, L.T., B. Orr, G. Rajendraprasad, A.J. Pereira, C. Lemos, J.T. Lima, C. Guasch Boldú, J.G. Ferreira, M. Barisic, and H. Maiato. 2020. α-Tubulin detyrosination impairs mitotic error correction by suppressing MCAK centromeric activity. *J Cell Biol*. 219.

Gill, S.R., T.A. Schroer, I. Szilak, E.R. Steuer, M.P. Sheetz, and D.W. Cleveland. 1991. Dynactin, a conserved, ubiquitously expressed component of an activator of vesicle motility mediated by cytoplasmic dynein. *J Cell Biol*. 115:1639-1650.

Goedhart, J. 2019. PlotsOfDifferences – a web app for the quantitative comparison of unpaired data. *bioRxiv*:578575.

Grotjahn, D.A., S. Chowdhury, Y. Xu, R.J. McKenney, T.A. Schroer, and G.C. Lander. 2018. Cryo-electron tomography reveals that dynactin recruits a team of dyneins for processive motility. *Nat Struct Mol Biol*. 25:203-207.

Gundersen, G.G., S. Khawaja, and J.C. Bulinski. 1987. Postpolymerization detyrosination of alpha-tubulin: a mechanism for subcellular differentiation of microtubules. *J Cell Biol*. 105:251-264.

372 Hancock, W.O. 2014. Bidirectional cargo transport: moving beyond tug of war. *Nat Rev Mol Cell*
373 *Biol*. 15:615-628.
374 Hendricks, A.G., E. Perlson, J.L. Ross, H.W. Schroeder, 3rd, M. Tokito, and E.L. Holzbaur. 2010.
375 Motor coordination via a tug-of-war mechanism drives bidirectional vesicle transport. *Curr*
376 *Biol*. 20:697-702.
377 Hirokawa, N., Y. Noda, Y. Tanaka, and S. Niwa. 2009. Kinesin superfamily motor proteins and
378 intracellular transport. *Nat Rev Mol Cell Biol*. 10:682-696.
379 Ide, A.H., K.F. DeLuca, O. Wiggan, S.M. Markus, and J.G. DeLuca. 2023. The role of kinetochore
380 dynein in checkpoint silencing is restricted to disassembly of the corona. *Mol Biol Cell*.
381 34:ar76.
382 Kobayashi, T., and T. Murayama. 2009. Cell cycle-dependent microtubule-based dynamic
383 transport of cytoplasmic dynein in mammalian cells. *PLoS One*. 4:e7827.
384 Maeder, C.I., K. Shen, and C.C. Hoogenraad. 2014. Axon and dendritic trafficking. *Curr Opin*
385 *Neurobiol*. 27:165-170.
386 Mann, B.J., and P. Wadsworth. 2018. Distribution of Eg5 and TPX2 in mitosis: Insight from
387 CRISPR tagged cells. *Cytoskeleton (Hoboken)*. 75:508-521.
388 McKenney, R.J., W. Huynh, M.E. Tanenbaum, G. Bhabha, and R.D. Vale. 2014. Activation of
389 cytoplasmic dynein motility by dynactin-cargo adapter complexes. *Science*. 345:337-341.
390 McKenney, R.J., W. Huynh, R.D. Vale, and M. Sirajuddin. 2016. Tyrosination of α-tubulin controls
391 the initiation of processive dynein-dynactin motility. *Embo j*. 35:1175-1185.
392 Moyer, T.C., and A.J. Holland. 2015. Generation of a conditional analog-sensitive kinase in
393 human cells using CRISPR/Cas9-mediated genome engineering. *Methods Cell Biol*.
394 129:19-36.
395 Nirschl, J.J., M.M. Magiera, J.E. Lazarus, C. Janke, and E.L. Holzbaur. 2016. α-Tubulin
396 Tyrosination and CLIP-170 Phosphorylation Regulate the Initiation of Dynein-Driven
397 Transport in Neurons. *Cell Rep*. 14:2637-2652.
398 Peris, L., M. Thery, J. Fauré, Y. Saoudi, L. Lafanechère, J.K. Chilton, P. Gordon-Weeks, N.
399 Galjart, M. Bornens, L. Wordeman, J. Wehland, A. Andrieux, and D. Job. 2006. Tubulin
400 tyrosination is a major factor affecting the recruitment of CAP-Gly proteins at microtubule
401 plus ends. *J Cell Biol*. 174:839-849.
402 Pfister, K.K., E.M. Fisher, I.R. Gibbons, T.S. Hays, E.L. Holzbaur, J.R. McIntosh, M.E. Porter,
403 T.A. Schroer, K.T. Vaughan, G.B. Witman, S.M. King, and R.B. Vallee. 2005. Cytoplasmic
404 dynein nomenclature. *J Cell Biol*. 171:411-413.
405 Ran, F.A., P.D. Hsu, J. Wright, V. Agarwala, D.A. Scott, and F. Zhang. 2013. Genome engineering
406 using the CRISPR-Cas9 system. *Nat Protoc*. 8:2281-2308.
407 Reck-Peterson, S.L., W.B. Redwine, R.D. Vale, and A.P. Carter. 2018. The cytoplasmic dynein
408 transport machinery and its many cargoes. *Nat Rev Mol Cell Biol*. 19:382-398.
409 Roberts, B., A. Haupt, A. Tucker, T. Grancharova, J. Arakaki, M.A. Fuqua, A. Nelson, C. Hookway,
410 S.A. Ludmann, I.A. Mueller, R. Yang, R. Horwitz, S.M. Rafelski, and R.N. Gunawardane.
411 2017. Systematic gene tagging using CRISPR/Cas9 in human stem cells to illuminate cell
412 organization. *Mol Biol Cell*. 28:2854-2874.
413 Roll-Mecak, A. 2020. The Tubulin Code in Microtubule Dynamics and Information Encoding. *Dev*
414 *Cell*. 54:7-20.
415 Rusan, N.M., C.J. Fagerstrom, A.M. Yvon, and P. Wadsworth. 2001. Cell cycle-dependent
416 changes in microtubule dynamics in living cells expressing green fluorescent protein-alpha
417 tubulin. *Mol Biol Cell*. 12:971-980.
418 Schlager, M.A., H.T. Hoang, L. Urnavicius, S.L. Bullock, and A.P. Carter. 2014. In vitro
419 reconstitution of a highly processive recombinant human dynein complex. *Embo j*.
420 33:1855-1868.
421 Schroer, T.A., and M.P. Sheetz. 1991. Two activators of microtubule-based vesicle transport. *J*
422 *Cell Biol*. 115:1309-1318.

423 Schuster, M., R. Lipowsky, M.A. Assmann, P. Lenz, and G. Steinberg. 2011. Transient binding of
424 dynein controls bidirectional long-range motility of early endosomes. *Proc Natl Acad Sci*
425 *U S A*. 108:3618-3623.
426 Sheridan, R.M., and D.L. Bentley. 2016. Selectable one-step PCR-mediated integration of a
427 degron for rapid depletion of endogenous human proteins. *Biotechniques*. 60:69-74.
428 Sirajuddin, M., L.M. Rice, and R.D. Vale. 2014. Regulation of microtubule motors by tubulin
429 isotypes and post-translational modifications. *Nat Cell Biol*. 16:335-344.
430 Splinter, D., D.S. Razafsky, M.A. Schlager, A. Serra-Marques, I. Grigoriev, J. Demmers, N.
431 Keijzer, K. Jiang, I. Poser, A.A. Hyman, C.C. Hoogenraad, S.J. King, and A. Akhmanova.
432 2012. BICD2, dynactin, and LIS1 cooperate in regulating dynein recruitment to cellular
433 structures. *Mol Biol Cell*. 23:4226-4241.
434 Stewart-Ornstein, J., and G. Lahav. 2016. Dynamics of CDKN1A in Single Cells Defined by an
435 Endogenous Fluorescent Tagging Toolkit. *Cell Rep*. 14:1800-1811.
436 Urnavicius, L., C.K. Lau, M.M. Elshenawy, E. Morales-Rios, C. Motz, A. Yildiz, and A.P. Carter.
437 2018. Cryo-EM shows how dynactin recruits two dyneins for faster movement. *Nature*.
438 554:202-206.
439 Urnavicius, L., K. Zhang, A.G. Diamant, C. Motz, M.A. Schlager, M. Yu, N.A. Patel, C.V. Robinson,
440 and A.P. Carter. 2015. The structure of the dynactin complex and its interaction with
441 dynein. *Science*. 347:1441-1446.
442 Vale, R.D. 1987. Intracellular Transport Using Microtubule-Based Motors. *Annual Review of Cell*
443 *Biology*. 3:347-378.
444 Vaughan, K.T., S.H. Tynan, N.E. Faulkner, C.J. Echeverri, and R.B. Vallee. 1999. Colocalization
445 of cytoplasmic dynein with dynactin and CLIP-170 at microtubule distal ends. *J Cell Sci*.
446 112 (Pt 10):1437-1447.
447 Vaughan, P.S., P. Miura, M. Henderson, B. Byrne, and K.T. Vaughan. 2002. A role for regulated
448 binding of p150(Glued) to microtubule plus ends in organelle transport. *J Cell Biol*.
449 158:305-319.
450 Walker, R.A., E.T. O'Brien, N.K. Pryer, M.F. Soboeiro, W.A. Voter, H.P. Erickson, and E.D.
451 Salmon. 1988. Dynamic instability of individual microtubules analyzed by video light
452 microscopy: rate constants and transition frequencies. *J Cell Biol*. 107:1437-1448.
453 Webster, D.R., J. Wehland, K. Weber, and G.G. Borisy. 1990. Detyrosination of alpha tubulin
454 does not stabilize microtubules in vivo. *J Cell Biol*. 111:113-122.
455 Ye, A.A., and T.J. Maresca. 2018. Measuring mitotic forces. *Methods Cell Biol*. 144:165-184.
456 Ye, A.A., V. Verma, and T.J. Maresca. 2018. NOD is a plus end-directed motor that binds EB1
457 via a new microtubule tip localization sequence. *J Cell Biol*. 217:3007-3017.
458 Zhang, K., H.E. Foster, A. Rondelet, S.E. Lacey, N. Bahi-Buisson, A.W. Bird, and A.P. Carter.
459 2017. Cryo-EM Reveals How Human Cytoplasmic Dynein Is Auto-inhibited and Activated.
460 *Cell*. 169:1303-1314.e1318.

461

462

463 **FIGURE LEGENDS**

464 **Figure 1. Dynein tip-tracks on polymerizing MTs and walks processively at high velocities**
465 **in interphase HeLa cells. (A)** Representative spinning disc confocal time-lapse of a DHC-EGFP-
466 expressing HeLa cell showing robust tip-tracking. Zoomed views of the numbered boxed regions
467 are shown to the right with kymographs of the tip-tracking events highlighted with yellow arrows
468 in the zoomed panels. **(B)** Representative TIRFM time-lapse of a DHC-EGFP-expressing HeLa
469 cell showing the tip-tracking population. Zoomed views of the numbered boxed regions are shown
470 with kymographs of the tip-tracking events highlighted with yellow arrows. **(C)** Still frame from a
471 representative TIRFM time-lapse of a DHC-EGFP-expressing HeLa cell treated with SiR-Tubulin.
472 In the merge image DHC is green and Sir-Tubulin labeled MTs are magenta. **(D)** Still frame from
473 a representative high temporal resolution (5 fps) TIRFM time-lapse of a DHC-EGFP-expressing
474 HeLa cell treated with SiR-Tubulin. Boxed region is shown as a zoomed inset in the lower panel
475 with the track of a motile DHC puncta highlighted in green. **(E)** Representative kymographs of
476 motile puncta spanning the range of measured velocities (Vel) and run lengths (RL). **(F)**
477 Distribution of DHC velocities (n = 100 puncta). **(G)** Distribution of DHC run lengths (n = 81
478 puncta). **(H)** Distribution of DHC run times (n = 81 puncta). Scale bars, 10 μm (A-D); 1 μm (all
479 insets), 10 μm (horizontal); 1 min (vertical) in the kymographs in A and B; and 1 μm (horizontal);
480 1 second (vertical) in E. Displayed times are min:sec.

481

482 **Figure 2. The dynactin complex component p50 tip-tracks on polymerizing MTs and walks**
483 **processively at high velocities in interphase HeLa cells. (A)** Still frames from a representative
484 spinning disc confocal time-lapse of a p50-EGFP-expressing HeLa cell. Zoomed view of the
485 boxed region is shown with a kymograph of the tip-tracking event highlighted with the yellow
486 arrow. **(B)** Still frames from a representative TIRFM time-lapse of a p50-EGFP-expressing HeLa
487 cell showing the tip-tracking population. Zoomed view of the boxed region is shown with a

488 kymograph of the tip-tracking event highlighted by the yellow arrow. **(C)** Still frame from a
489 representative TIRFM time-lapse of a p50-EGFP-expressing HeLa cell treated with SiR-Tubulin.
490 In the merge image p50 is green and Sir-Tubulin labeled MTs are magenta. **(D)** Representative
491 kymographs of motile p50 puncta spanning the range of measured velocities (Vel) and run lengths
492 (RL). **(E)** Distribution of p50 velocities (n = 44 puncta). **(F)** Distribution of p50 run lengths (n = 41
493 puncta). **(G)** Distribution of p50 run times (n = 41 puncta). Scale bars, 10 μm (A-C); 1 μm (all
494 insets), 5 μm (horizontal); 1 min (vertical) in the kymographs in A and B; and 1 μm (horizontal); 1
495 second (vertical) in D. Displayed times are min:sec.

496

497 **Figure 3. Motile DHC and p50 puncta exhibit identical motility parameters but different**
498 **fluorescent intensities. (A-C)** Box and whisker plots of DHC and p50 velocities (A), run lengths
499 (B), and run times (C). **(D-F)** Distributions of kinesin-1-EGFP (D), DHC-EGFP (E), and p50-EGFP
500 background corrected fluorescence intensities. The dashed line in each histogram denotes the
501 mean value of the kinesin-1-EGFP data set. **(G)** Box and whisker plots of the kinesin-1, DHC, and
502 p50 fluorescence intensities. **(H)** PCR of genomic DNA from the DCH-EGP clone used in this
503 study using PCR primers flanking the integration site of the repair cassette. The upper band was
504 extracted and subjected to sequencing the results of which are shown in Figure 1 – supplemental
505 figure 1. **(I)** Western blot for p50 of cell lysates from the parental HeLa cell line and the p50-EGFP
506 clone used in this study. The tagged p50 runs ~30 kDa larger than the untagged p50 and is
507 expressed at ~5-6-fold lower levels than the endogenous p50. In the box and whisker plots,
508 whiskers indicate min-max, box is 25th-75th percentile, and bar is median. The reported p-values
509 were determined by a randomization method: n.s. is not significant ($p > 0.05$).

510

511 **SUPPLEMENTAL MATERIALS**

512 **Supplemental Figures**

513 **Figure 1 – figure supplement 1. Repair cassette for generating the DHC-EGFP CRISPR-**
514 **engineered HeLa cell line with sequencing trace showing its integration at the dynein**
515 **heavy chain (DYNC1H1) gene locus.**

516

517 **Supplemental Videos**

518 **Video 1. Spinning disk confocal time-lapse of a DHC-EGFP CRISPR-engineered interphase**
519 **HeLa cell.** Zoomed views of the boxed regions in the upper left panel are shown in the right
520 panels. Displayed times are min:sec. Scale bars, 10 µm (upper left panel) and 1 µm (right panels).
521 Relates to Fig. 1A.

522

523 **Video 2. TIRFM time-lapse of a DHC-EGFP CRISPR-engineered interphase HeLa cell.**
524 Displayed times are min:sec. Scale bar, 10 µm. Relates to Fig. 1B.

525

526 **Video 3. TIRFM time-lapse of a DHC-EGFP (green) CRISPR-engineered interphase HeLa**
527 **cell treated with SiR-Tubulin (magenta).** Displayed times are min:sec. Scale bar, 10 µm.
528 Relates to Fig. 1C.

529

530 **Video 4. High temporal-resolution (5 frames per second) TIRFM time-lapse of a DHC-EGFP**
531 **CRISPR-engineered interphase HeLa cell treated with SiR-Tubulin.** The boxed regions
532 highlight motile DHC puncta. Displayed times are sec:millisec. Scale bar, 1 µm. Relates to Fig.
533 1C.

534

535 **Video 5. Spinning disk confocal time-lapse of a p50-EGFP CRISPR-engineered interphase**
536 **HeLa cell.** Displayed times are min:sec. Scale bar, 10 μm. Relates to Fig. 2A.
537
538 **Video 6. TIRFM time-lapse of a p50-EGFP CRISPR-engineered interphase HeLa cell.**
539 Displayed times are min:sec. Scale bar, 10 μm. Relates to Fig. 2B.
540
541 **Video 7. TIRFM time-lapse of a p50-EGFP (green) CRISPR-engineered interphase HeLa cell**
542 **treated with SiR-Tubulin (magenta).** Displayed times are min:sec. Scale bar, 10 μm. Relates to
543 Fig. 2C.
544
545

Figure 1

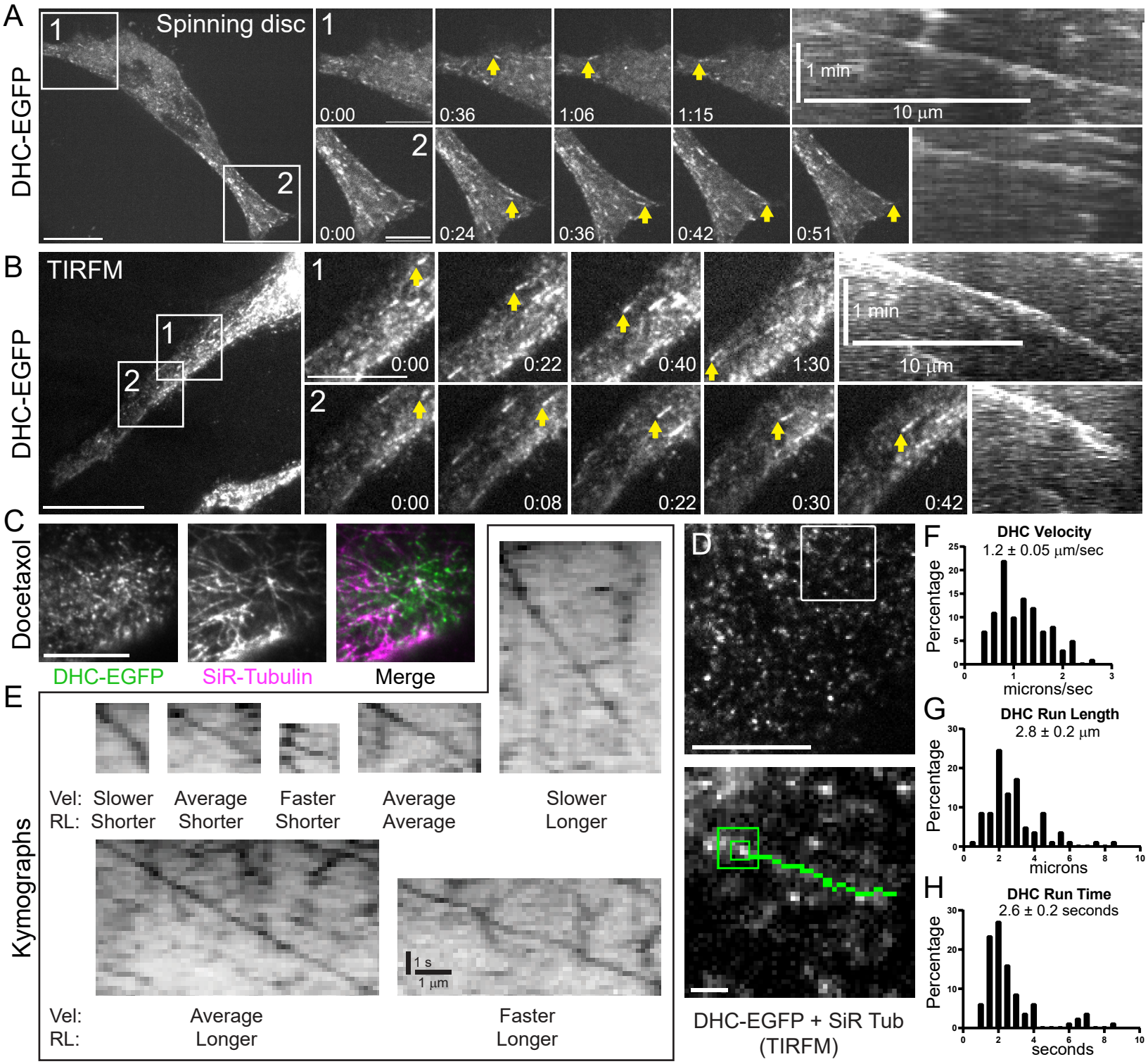
A
DHC-EGFP
Spinning disc
1
2
0:00
0:36
1:06
1:15
1 min
10 µm
0:00
0:24
0:36
0:42
0:51
B
DHC-EGFP
TIRFM
1
2
0:00
0:22
0:40
1:30
1 min
10 µm
0:00
0:08
0:22
0:30
0:42
C
Docetaxol
DHC-EGFP
SiR-Tubulin
Merge
D
DHC-EGFP + SiR Tub
(TIRFM)
E
Kymographs
Vel: Slower Average Faster Average Slower
RL: Shorter Shorter Shorter Average Longer
1 s
1 µm
Vel: Average Faster
RL: Longer Longer
F
DHC Velocity
1.2 ± 0.05 µm/sec
Percentage
microns/sec
G
DHC Run Length
2.8 ± 0.2 µm
Percentage
microns
H
DHC Run Time
2.6 ± 0.2 seconds
Percentage
seconds

Figure 2

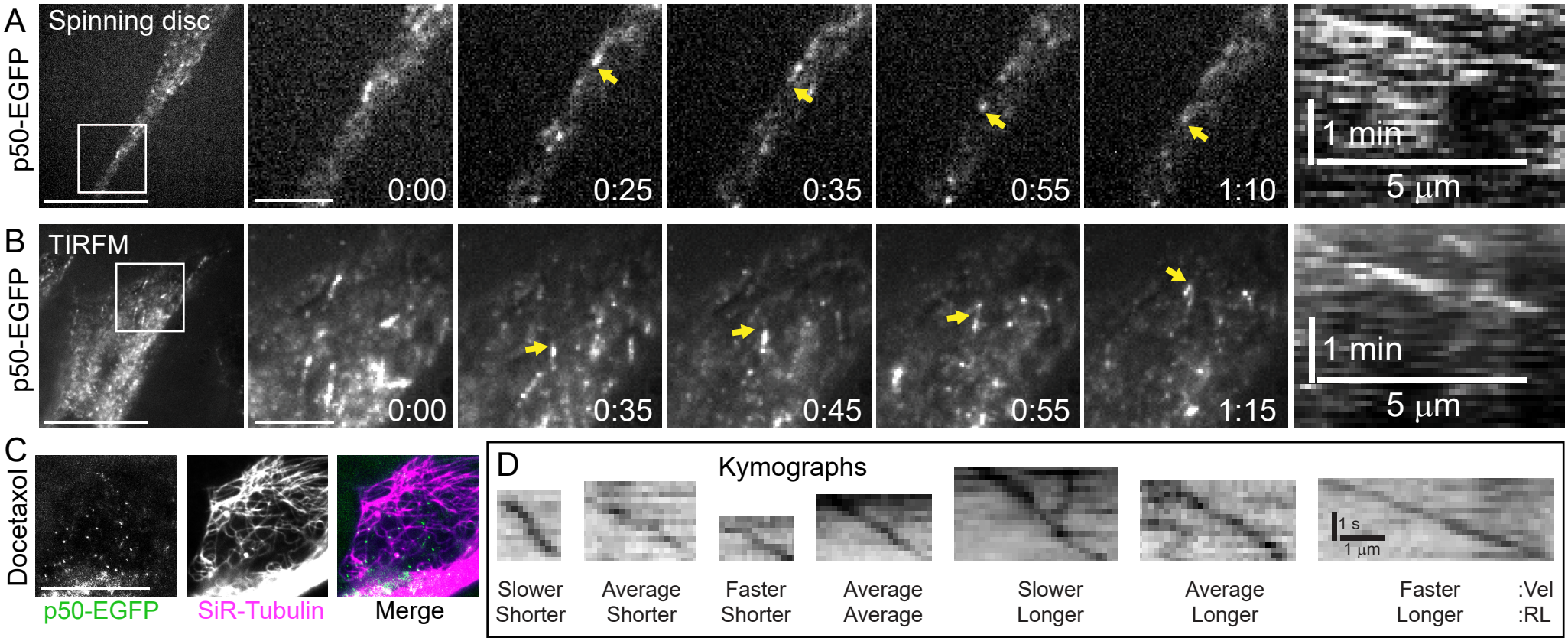
A
p50-EGFP
Spinning disc
0:00
0:25
0:35
0:55
1:10
1 min
5 µm
B
p50-EGFP
TIRFM
0:00
0:35
0:45
0:55
1:15
1 min
5 µm
C
Docetaxol
p50-EGFP
SiR-Tubulin
Merge
D
Kymographs
1 s
1 µm
Slower Shorter
Average Shorter
Faster Shorter
Average Average
Slower Longer
Average Longer
Faster Longer
:Vel
:RL

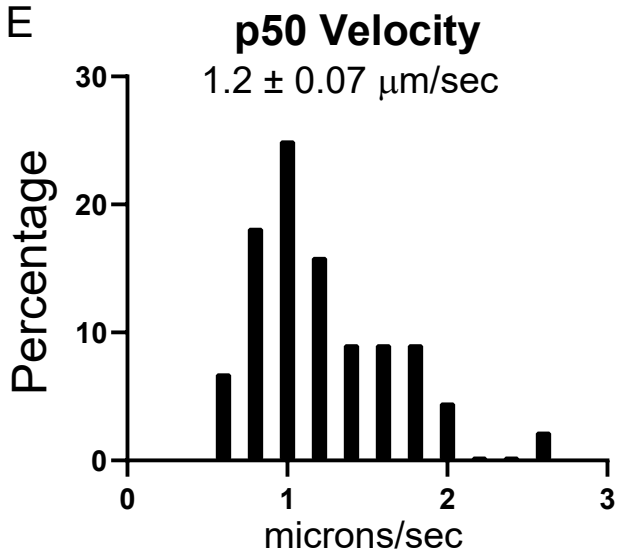
E
p50 Velocity
1.2 ± 0.07 µm/sec
Percentage
0
10
20
30
0
1
2
3
microns/sec

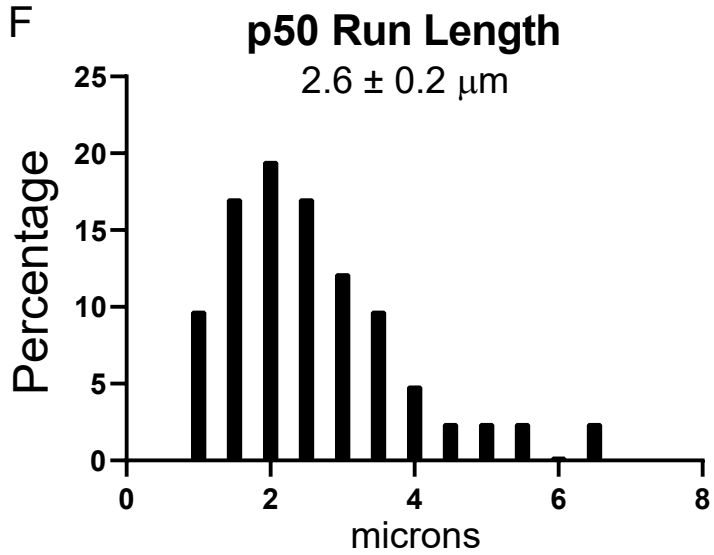
F
p50 Run Length
2.6 ± 0.2 µm
Percentage
0
5
10
15
20
25
0
2
4
6
8
microns

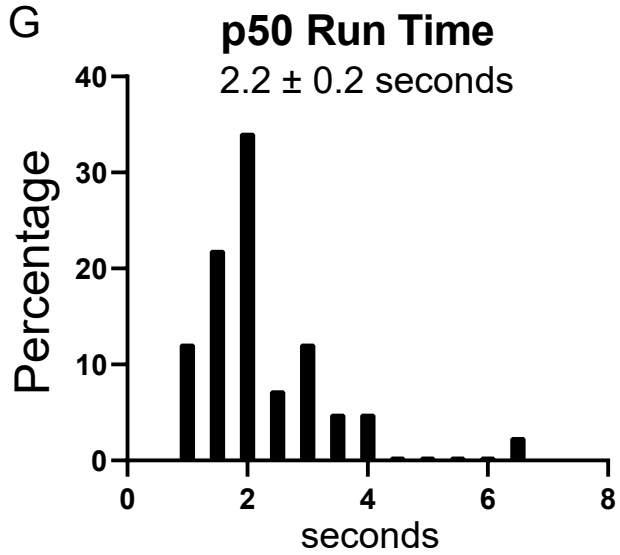
G
p50 Run Time
2.2 ± 0.2 seconds
Percentage
0
10
20
30
40
0
2
4
6
8
seconds

Figure 3

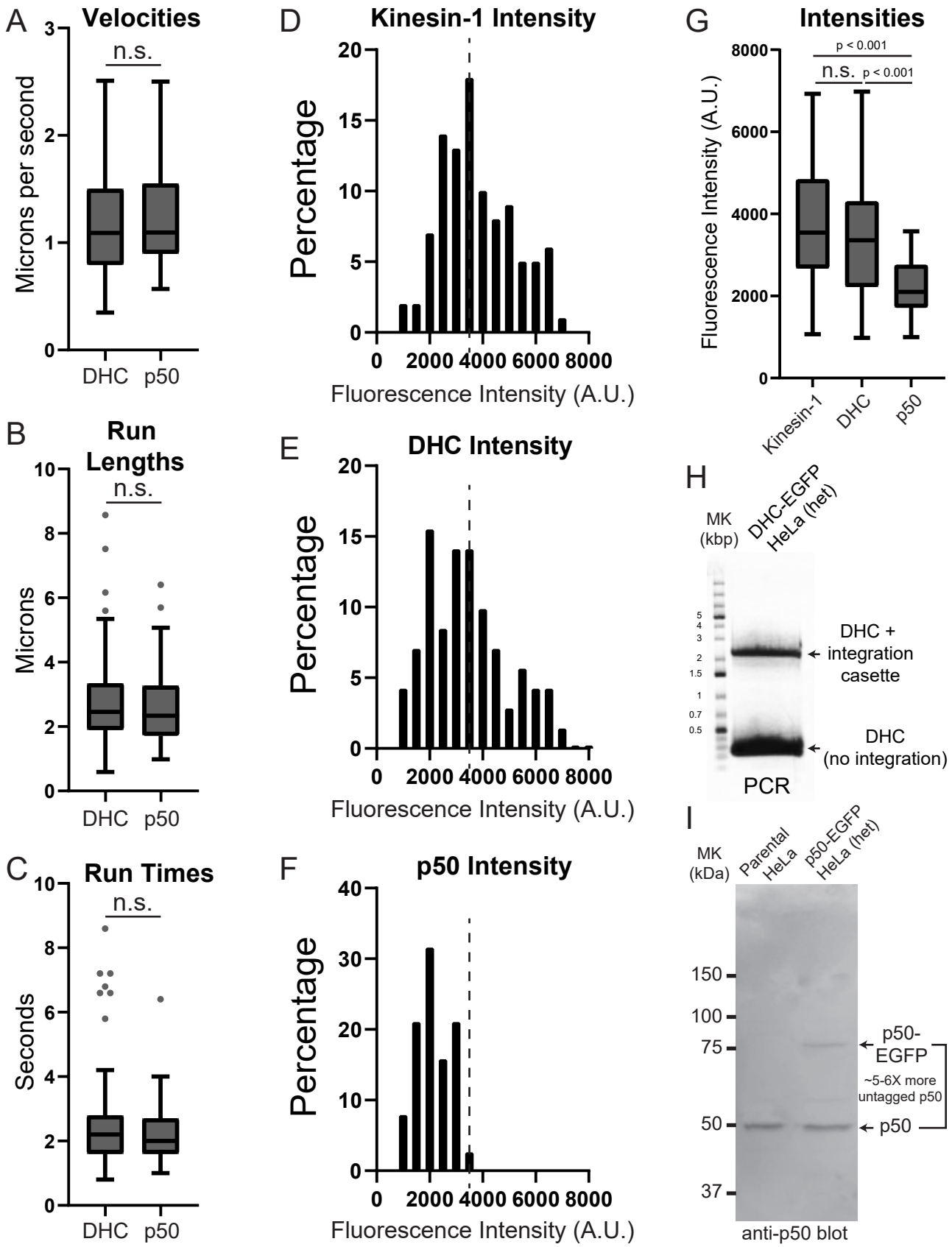
A
Velocities
n.s.
Microns per second
DHC
p50
B
Run Lengths
n.s.
Microns
DHC
p50
C
Run Times
n.s.
Seconds
DHC
p50
D
Kinesin-1 Intensity
Percentage
Fluorescence Intensity (A.U.)
E
DHC Intensity
Percentage
Fluorescence Intensity (A.U.)
F
p50 Intensity
Percentage
Fluorescence Intensity (A.U.)
G
Intensities
p < 0.001
n.s.
p < 0.001
Fluorescence Intensity (A.U.)
Kinesin-1
DHC
p50
H
MK (kbp)
DHC-EGFP HeLa (het)
DHC + integration casette
DHC (no integration)
PCR
I
MK (kDa)
Parental HeLa
p50-EGFP HeLa (het)
150
100
75
50
37
p50-EGFP
~5-6X more untagged p50
p50
anti-p50 blot
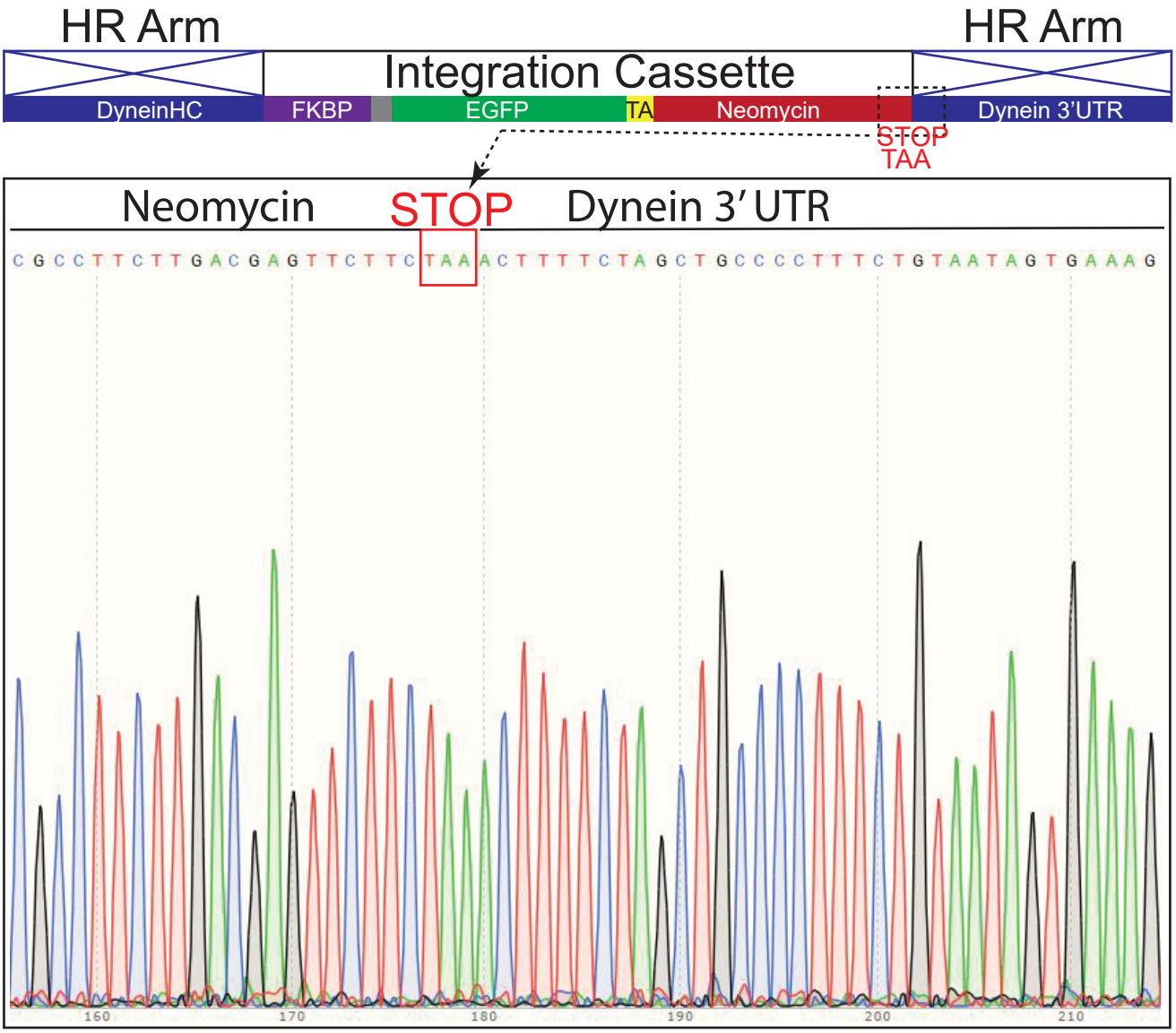
Figure 1 - figure supplement 1